Effect of nanosilica addition on the physicomechanical properties, pore morphology, and phase transformation of freeze cast hydroxyapatite scaffolds

Seyed Mohammad Hossein Ghazanfari · Ali Zamanian

Received: 5 January 2014/Accepted: 18 April 2014/Published online: 8 May 2014 © Springer Science+Business Media New York 2014

Abstract Freeze casting technique is a simple and effective method for the fabrication of porous ceramic structures. The objective of this work is to study the production and characterization of hydroxyapatite/nanosilica (HA/nSiO₂) scaffolds fabricated through this method. In the experimental procedure, the solidified samples were prepared by slurries containing different concentration of HA and nSiO₂ followed by sintering procedure at 1200 and 1350 °C. The phase composition, microstructure, and compressive strength of the scaffolds were characterized by X-ray diffraction, scanning electron microscopy, and mechanical strength test. It was found that the porosity of the scaffolds was in the range of 30-86.5 % and the value of compressive strengths lied between 0.16 and 71.96 MPa which were influenced by nSiO₂ content, cooling rate, and sintering temperature. With respect to porosity, pore size, and compressive strength, the scaffolds with 5 % nSiO₂, the cooling rate of 1 °C/min and the sintering temperature of 1350 °C showed preferable results for bone tissue engineering applications.

Introduction

For decades, the scientists have conducted multifarious researches to enhance the quality of human life and health care system. One of them has been repairing large bone defects which are not normally regenerated by normal bone remodeling process, happening by natural processes or other reasons [1, 2]. Materials used in the regeneration of

S. M. H. Ghazanfari · A. Zamanian (☒)
Nanotechnology & Advanced Materials Department, Materials & Energy Research Center, P.O. Box 13145-1659, Karaj, Iran e-mail: a-zamanian@merc.ac.ir



fully or partially damaged bone are known as "biomaterials" [3, 4]. Bioceramics, an important class of biomaterials, can be appropriately utilized in orthopedic and dental surgery due to their outstanding properties like high biocompatibility and stability [5, 6]. Among these, calcium phosphate-based biomaterials especially hydroxyapatite (HA) and tricalcium phosphate (TCP), or the combination of these two biomaterials have received a great deal of attention for using in bone regeneration due to their bioactivity, osteoconductivity, and similar composition to the natural hard tissues [7–10]. A large number of studies have been devoted to achieve proper phase composition and mechanical strength in these bioceramics. Different kinds of materials such as zirconia, alumina (Al₂O₃), silica (SiO₂), and titania have been employed for this purpose [11–14]. Normally, HA decomposes to TCP around 1350-1400 °C but the addition of these materials can lead to partial or complete decomposition of HA into TCP at lower temperatures [15–17]. Many studies have revealed that TCP is more degradable than HA [7]. However, low mechanical strength is a shortcoming for TCP [18]. On the other hand, possible formation of strong reinforcing agent in the matrix of HA/TCP as a result of reaction between HA and these materials can be a promising approach to improve the mechanical strength [19-21]. For example, Juang et al. [22] investigated the phase transformation and mechanical strength of HA/Al₂O₃ composites. They reported that HA decomposed to TCP, and CaAl₂O₄ was formed as a reinforcing phase. They showed that the mechanical strength of the composites increased after addition of certain amount of A1₂O₃. Recently, An et al. [23] studied the physical properties and cellular compatibility of porous zirconia/HA scaffolds, and indicated that the compressive strength of the scaffolds was improved by increasing the zirconia concentration due to CaZrO₃ formation, while decomposition of HA to TCP happened. They also informed that the cell adhesion and proliferation in the zirconia/HA scaffolds was significantly enhanced compared to the zirconia-based scaffolds. Among these materials, SiO₂ has been mostly used to enhance the biological behavior of HA ceramics than the mechanical properties that it could bring [13, 24–26].

These fabricated composites are used in dense, granular, and porous forms [27-29]. The porous forms of these composites could provide notable features such as possibility of appropriate osteoconduction and consequently bone regeneration [30, 31]. Several fabrication techniques such as polymer sponge method, gel casting, slip casting, starch consolidation, microwave processing, and freeze casting have been used to produce porous structures [32-37]. Among these methods, freeze casting has attracted much attention due to its superior advantages such as simplicity, low shrinkage in forming process, possibility of controlling the porosity, interconnectivity, and relatively good mechanical strength [38-41]. Various additives have been also utilized to enhance the properties of HA-based scaffolds produced through the freeze casting method [42]. In our previous work, we studied the effect of nano-alumina (nAl₂O₃) on the microstructural and mechanical properties of HA scaffold [43]. We reported that the addition of nAl₂O₃ decomposed HA to TCP, and as a result, calcium aluminate formed as a reinforcement phase. In addition, it increased the pore size along with the compressive strength [43]. In another work, Blindow et al. [24] investigated the influence of nanosilica (nSiO₂) addition on the characteristics of HA scaffolds. They reported that 1 and 1.7 wt% nSiO₂ addition caused a partial phase transformation of HA to β-TCP and reduced the shrinkage after sintering. Moreover, it seemed to stimulate osteoblastlike cell responses [24]. However, they did not study the mechanical and structural properties of the scaffolds in these contents as well as the effect of more addition of nSiO₂. To our knowledge, there is no report on the effect of nSiO₂ on the structural and mechanical properties of HA scaffolds fabricated by freeze casting method. The object of this study is to investigate the phase transformation, structural, and mechanical characteristics of HA/nSiO₂ nanocomposite produced by freeze casting process.

Materials and methods

Scaffolds fabrication

The HA/nSiO₂ nanocomposite scaffolds with 15 vol% solid concentration were produced via an unidirectional freeze casting technique as reported in our previous work [43]. At first, to prepare stable slurries, a small amount of

Table 1 Slurry concentration, cooling rate, and sintering temperature of samples

Sample code	Micro-HA content (vol%)	Nanosilica content (vol%) (S_x)	Cooling rate (°C/min) (C_y)	Sintering temperature (°C) (Tz)
SxCyTz	99.5 99 98.5 95 90 85	0.5 1 1.5 5 10 15	1	1200 1350

That x is $nSiO_2$ content (vol%), y is cooling rate (°C/min), and z indicates the sintering temperature (°C). For example, S5C1T20 means: 5 vol% $nSiO_2$, cooling rate: 1 °C/min, sintering temperature: 1200 °C

dispersant agent (4 wt% of HA/nSiO₂ content) (Dolapix CE64, Zschimmer & Schwarz, Lahnstein, Germany) was added to distilled water. Then, different amounts of HA powder (2196, Merck KGaA, Darmstadt, Germany) and nSiO₂ (Sigma, USA, purity of 99.5 %) were added bit-bybit to the suspension, employing high speed magnetic stirring, as shown in Table 1. The mean particle size (d50) and specific surface area were 1.69 µm and 75.81 m²/g for HA, and 5–15 nm and 590–690 m^2/g for $nSiO_2$, respectively. All of these data were provided by the manufacturers. Then, the prepared slurries were ball-milled for 24 h with zirconia balls. After that, in order to strengthen the green samples and for the easy handling before sintering, polyvinyl alcohol (PVA, Mw = 15000, Merck, Darmstadt, Germany) was added as a binder at 4 wt% of the HA/nSiO₂ content. Before casting, air bubbles were removed by a vacuum oven at a pressure of 0.02 MPa for 20 min. The scaffolds were prepared using a setup as described previously [37]. Briefly, the slurries were poured into a PTFE mold, located on a cold finger, where the temperature was regulated using liquid nitrogen and a ring heater connected to a PID controller, and the temperature was monitored utilizing a PT thermocouple placed near the surface of the cold finger. The schematic of the applied freeze casting device is shown in Fig. 1. The slurries were poured into the PTFE mold at 5 °C, and different cooling rates were applied to solidify the samples (see Table 1). After that, the solidified samples were removed from the mold carefully and placed in a freeze dryer (FD-10, Pishtaz Engineering Co., Tehran, Iran) for 48 h to sublimate the ice crystals. After sublimation, the green bodies were sintered at different temperatures. All of the samples were heated to 600 °C at heating rate of 5 °C/min and kept for 1 h at this temperature. The samples were then heated to the ultimate sintering temperatures (Table 1) at the same heating rate and maintained for 2 h. The sintering cycles were



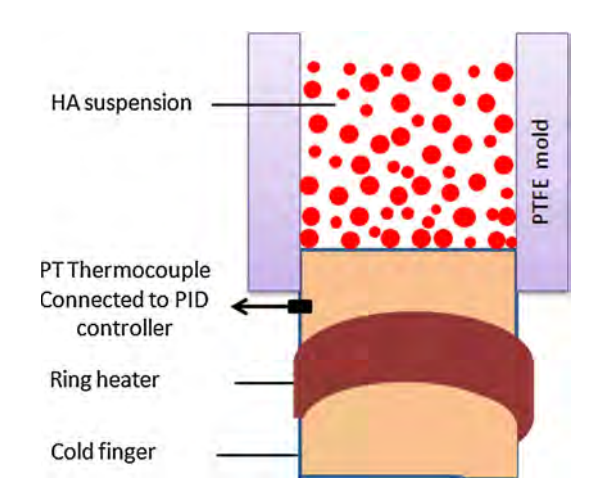


Fig. 1 Schematic of the freeze casting setup used in this study

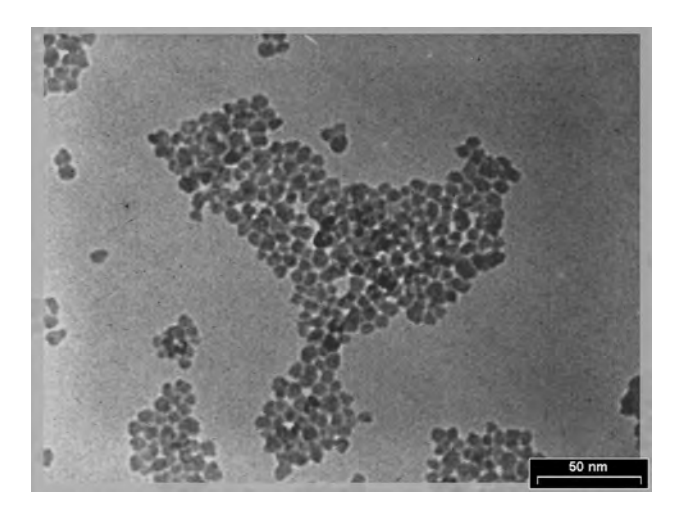


Fig. 2 TEM macrograph of nSiO₂ powder

completed with a cooling rate of 300 °C/h down to room temperature.

Characterization of the samples

Phase analysis

Phase analysis of the sintered $HA/nSiO_2$ nanocomposite scaffolds was conducted using a X-ray diffraction (XRD, Philips PW3710) with monochromatic Cu K α radiation under the operating conditions of 40 kV and 30 mA. Comparison of XRD patterns with JCPDS standards was carried out to identify the crystalline phases.

Structural characterization

The morphology of the nSiO₂ particles was analyzed by transmission electron microscopy (TEM). For this purpose,

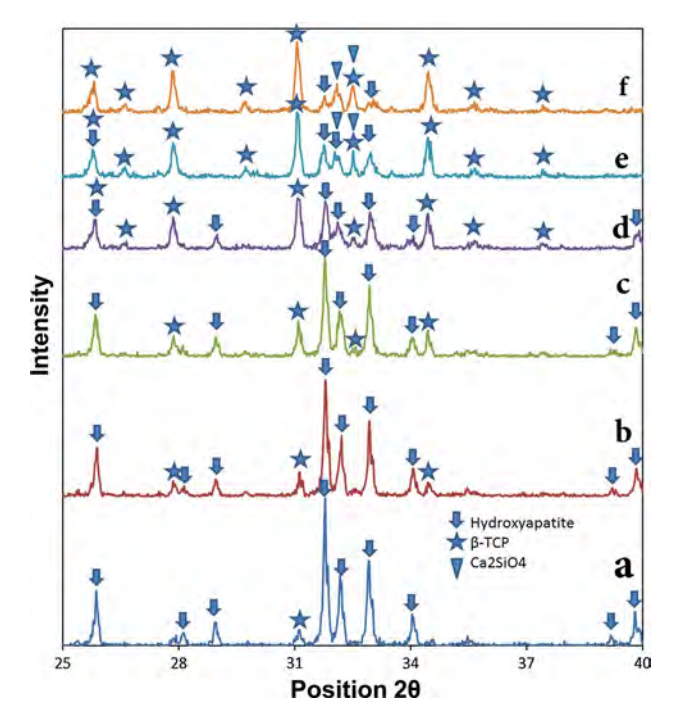


Fig. 3 XRD patterns of $HA/nSiO_2$ nanocomposites sintered at 1200 °C (a S0.5C1T20, b S1C1T20, c S1.5C1T20, d S5C1T20, e S10C1T20, f S15C1T20)

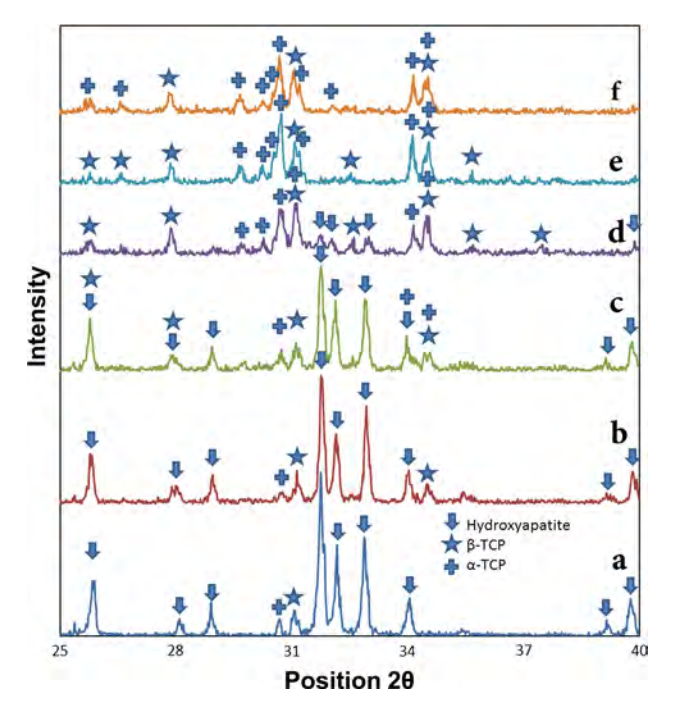


Fig. 4 XRD patterns of $HA/nSiO_2$ nanocomposites sintered at 1350 °C (a S0.5C1T35, b S1C1T35, c S1.5C1T35, d S5C1T35, e S10C1T35, f S15C1T35)

the powders were ultrasonically dispersed in ethanol to form a diluted suspension and then a few droplets were dropped on carbon-coated copper grids. The morphology



of the particles was observed by a TEM instrument (GM200PEG Philips), operated at an accelerating voltage of 200 kV. Also, scanning electron microscopy (SEM, Stereoscan S360-Leica Cambridge, England) was utilized to characterize the morphology and the microstructure of the scaffolds. Before scanning, the scaffolds were coated by a thin layer of gold for a better electrical conductivity.

Porosity and pore size of scaffolds

The total porosity of the sintered scaffolds (P) was determined by density measurement (ratio of weight to total volume, ρ_{scaffold}) and theoretical density (depending on the amount of HA and nSiO₂, ρ_{solid}) using [44]

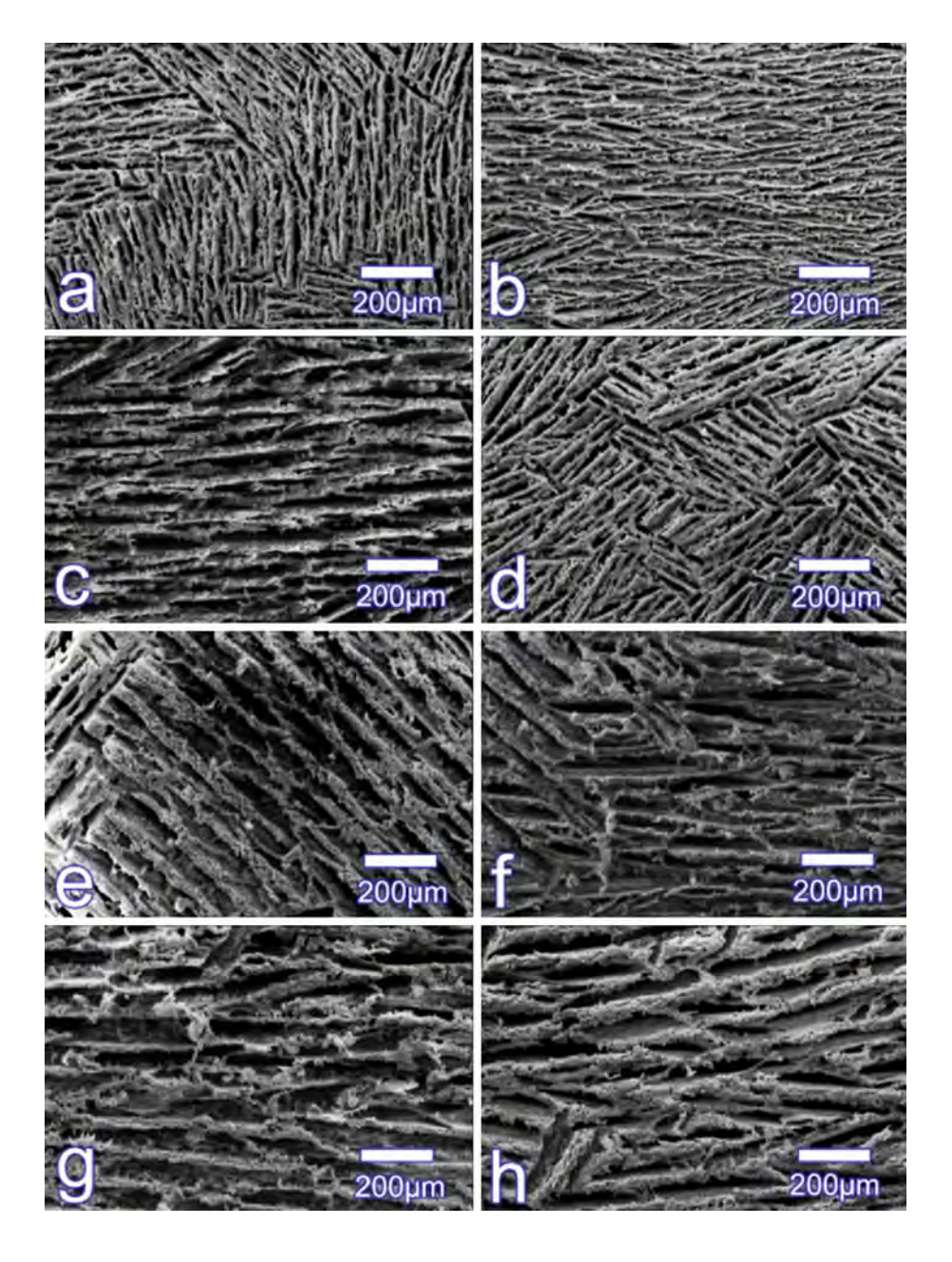
Fig. 5 Horizontal cross section SEM micrographs of HA/nSiO₂ nanocomposites at different cooling rates (a S0.5C1T20, b S0.5C4T20, c S5C1T20, d S5C4T20, e S10C1T20, f S10C4T20, g S15C1T20, h S15C4T20)

$$P = 1 - \rho_{\text{scaffold}} / \rho_{\text{solid}}. \tag{1}$$

At least five samples were calculated to obtain the average value and the standard deviation. Because the HA/nSiO₂ nanocomposites scaffolds were anisotropic, pore sizes were determined in both long and short axes. The pore sizes were measured using Quantify Image software and five samples were studied, with 50 measurements conducted for each sample.

Shrinkage measurement

The shrinkage volume was evaluated using the sample's volume before and after sintering [45]:





$$S_{\rm V} = (V_0 - V_{\rm f})/V_0 \tag{2}$$

in which, $S_{\rm V}$, V_0 , and $V_{\rm f}$ are the total shrinkage, initial, and final volumes, respectively. At least five samples were calculated to obtain the average value and the standard deviation.

Mechanical strength

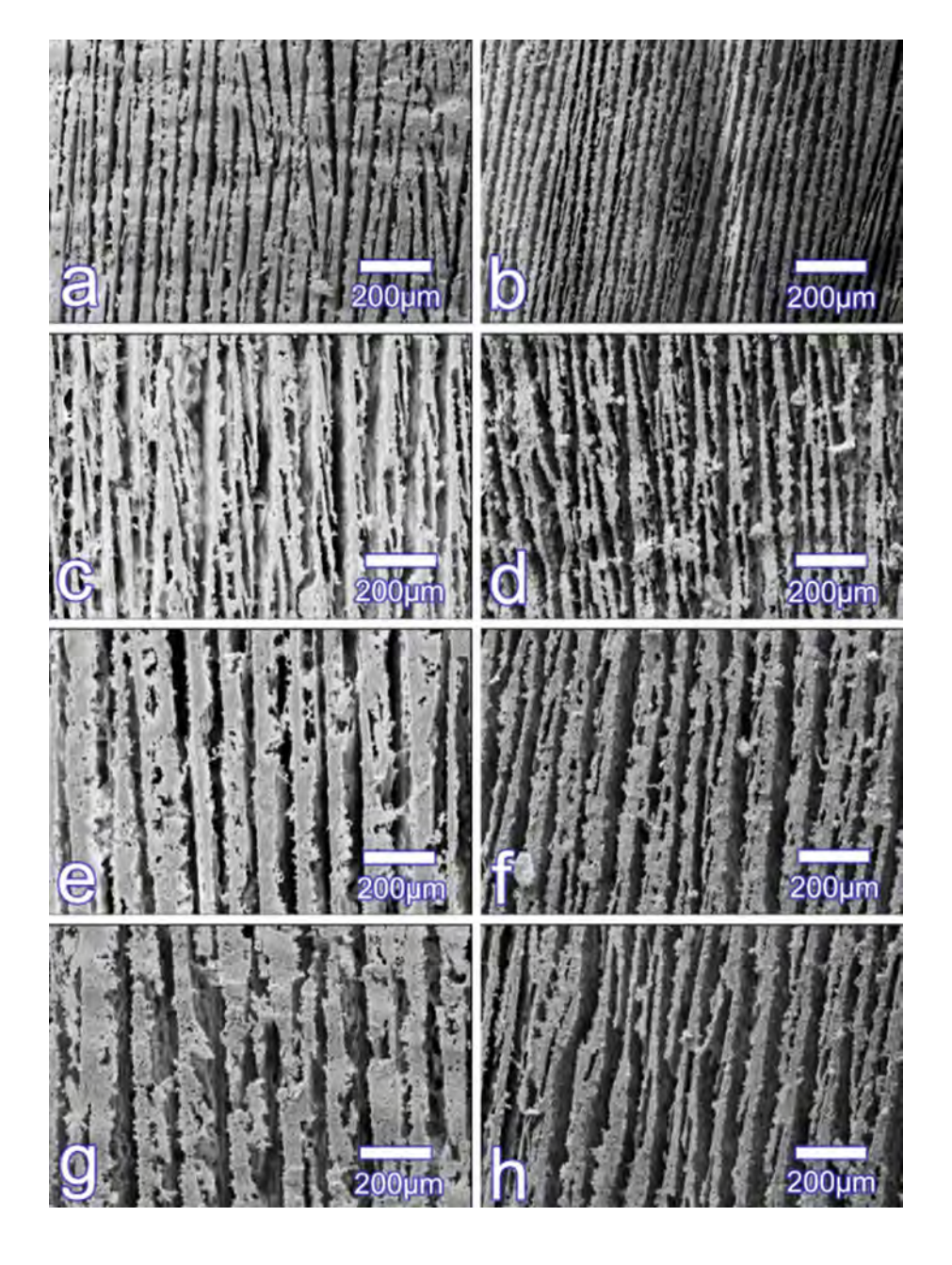
For the compressive strength measurements, the cylindrical scaffolds with diameters of 15 mm and heights of 20 mm were loaded with across-head speed of 0.5 mm/min using as crew-driven load frame (Instron 5565, Instron Corp., Canton, MA). The stress responses were monitored for at

Fig. 6 Vertical cross section SEM micrographs of HA/nSiO₂ nanocomposites at different cooling rates (a S0.5C1T20, b S0.5C4T20, c S5C1T20, d S5C4T20, e S10C1T20, f S10C4T20, g S15C1T20, h S15C4T20) least five samples of each group with different $HA/nSiO_2$ contents to obtain the average values and the standard deviations.

Results and discussion

TEM micrographs

Figure 2 shows the TEM image of nSiO₂ powder. As can be seen, the nSiO₂ grains are actually small and are not agglomerated. It can be seen that the nSiO₂ particles are homogeneous nanospheres, 5–15 nm in diameter.





Phase analysis

There are two key factors accounted for phase transformation study of HA/nSiO₂ nanocomposites. The first factor is the content of nSiO₂ in the samples. Figure 3a-f shows the XRD patterns of the HA/nSiO₂ nanocomposites with diverse HA/nSiO₂ contents sintered at 1200 °C (\$0.5C1T20, \$1C1T20, \$1.5C1T20, \$5C1T20, \$10C1T20, S15C1T20). As shown in Fig. 3a, a very small amount of HA was decomposed to β -TCP. This decomposition process in the samples containing 1 and 1.5 vol% nSiO₂ (S1C1T20, S1.5C1T20) were more noticeable, but still the main phase was HA. With further increase in nSiO2 content (S5C1T20, S10C1T20, S15C1T20), the main phase changed to \(\beta\)-TCP, but still a very small amount of HA remained in the samples. In all the XRD patterns, no significant peak associated with SiO2 could be detected. The absence of silica peaks in the XRD patterns clearly

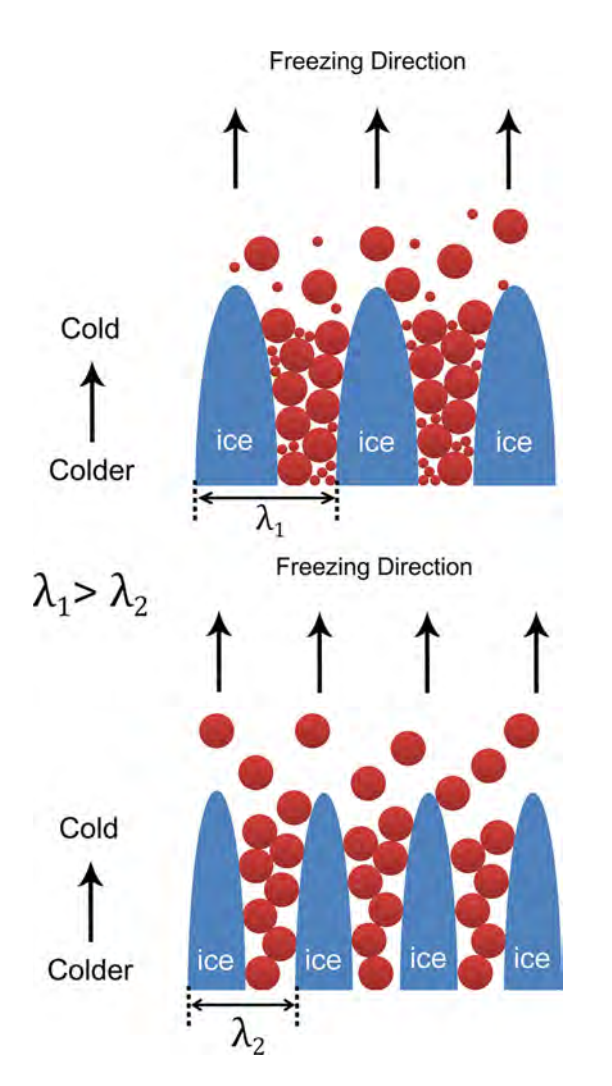


Fig. 7 2D schematic image of influence of $nSiO_2$ addition on ice formation, particles entrapment, and structural wavelength (λ)

revealed that SiO₂ reacted with HA and formed a new phase. Furthermore, some other peaks could be identified in the XRD patterns that belong to Ca₂SiO₄ (JCPDS#29-0369) which are approved by other studies [46]. Frequently, HA decomposes into TCP around 1350–1400 °C, as formerly described by the reaction shown in Eq. (3) or in some studies with Eq. (4) [15, 47]:

$$Ca_{10}(PO_4)_6(OH)_2 \rightarrow 3Ca_3(PO_4)_2 + CaO + H_2O$$
 (3)

$$Ca_{10}(PO_4)_6(OH)_2 \rightarrow 2Ca_3(PO_4)_2 + Ca_4P_2O_9 + H_2O.$$
 (4)

Nevertheless, HA/nSiO₂ nanocomposites are known to decompose at rather lower temperatures [24]. Moreover, the calcium silicate formation can be related to a reaction between SiO₂ and CaO (a dissociation product of HA) at temperatures lower than 1250 °C according to the CaO/SiO₂ equilibrium phase diagram [48]. The second factor is the sintering temperature. Figure 4a–f shows the XRD patterns of the HA/nSiO₂ nanocomposites with different HA/nSiO₂ contents sintered at 1350 °C (S0.5C1T35, S1C1T35, S1.5C1T35, S5C1T35, S10C1T35, S15C1T35). The phase transformation process at 1350 °C is rather different from 1200 °C. At this temperature, as shown in Fig. 4, HA was decomposed to α -TCP and β -TCP phases

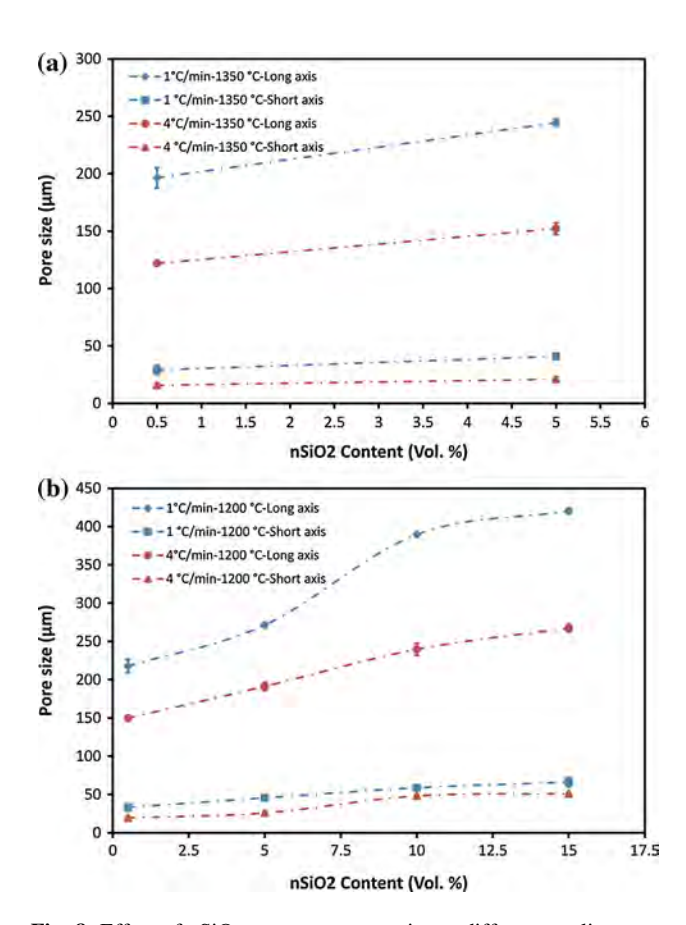


Fig. 8 Effect of $nSiO_2$ content on pore size at different cooling rates and sintering temperatures (a 1200 °C, b 1350 °C)



and such a decomposition increased with rise in content of $nSiO_2$. Similar to 1200 °C, dominant phase in the scaffolds containing 0.5–1.5 vol% $nSiO_2$ is HA and it changes to β -TCP in the sample with 5 vol% $nSiO_2$. It should be noted that for the scaffolds containing 10 and 15 vol% $nSiO_2$ in which HA was completely decomposed to α -TCP and β -TCP, the dominant phase is α -TCP. It is consistently well known that α -TCP is the high temperature (>1125 °C) tricalcium phosphate phase [49]. The CaO/P₂O₅ equilibrium phase diagram also confirms this issue [50]. According to Li et al. [13, 49], the sintering of pure HA in the presence of adequate SiO₂ may lead to form a unique crystalline Si-TCP phase (Ca₃(P_{0.9}Si_{0.1}O_{3.95})₂), which

possess a monoclinic structure similar to α -TCP with space group $P2_1/a$. Consequently, the present of the α -TCP phase might be a combination of α -TCP and Si-TCP phases. Also, the combination of CaO, P_2O_5 , and SiO $_2$ might form an amorphous phase based on Ca, Si, P, and O elements [13, 17]. Similar to 1200 °C, in all the XRD patterns at temperature of 1350 °C, no significant peak related to SiO $_2$ could be detected. In addition, no other crystalline phases containing Si element were recognized, and also, all the peaks in the XRD patterns have identified and there was no unknown peak. Moreover, there was an integral decrease in relative intensity of all the peaks by increasing the nSiO $_2$ content. Totally, regarding to all abovementioned reasons,

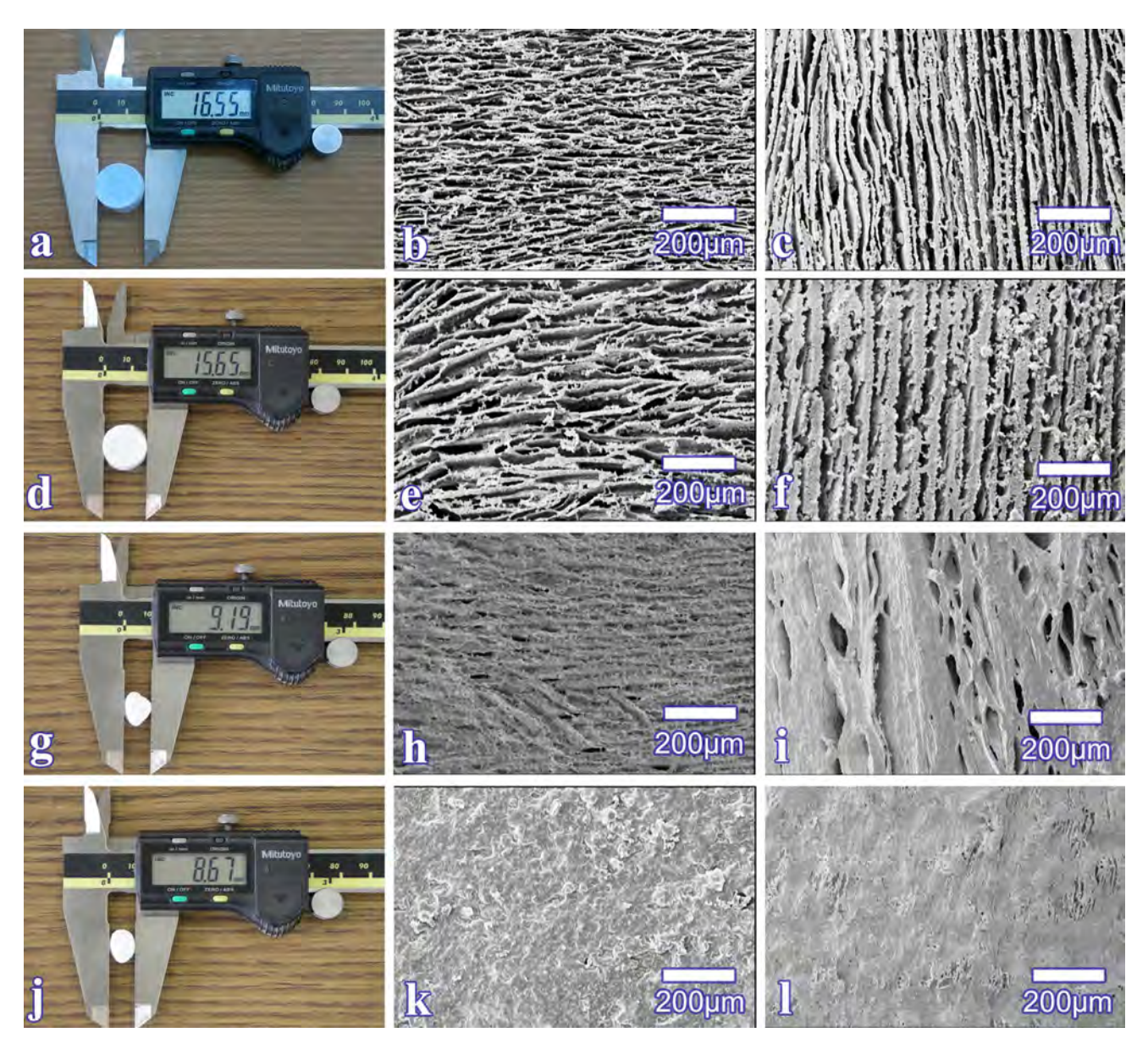


Fig. 9 HA/nSiO₂ nanocomposites sintered at 1350 °C and their horizontal and vertical cross section SEM micrographs (a-c S0.5C1T35; d-f S5C1T35; g-i S10C1T35, j-l S15C1T35)



it can be concluded that an amorphous phase (based on Ca, Si, P, and O) was formed or SiO₂ was remained amorphous till the end of the sintering process. Other evidential proofs will be presented in the following section.

Microstructural characterization

Figures 5 and 6 show the horizontal and vertical cross section SEM micrographs of HA/nSiO₂ nanocomposites, respectively, including different HA/nSiO₂ contents at different cooling rates (1 and 4 °C/min) sintered at 1200 °C. As it can be observed, two factors including cooling rate and particle size have noteworthy effects on the microstructure of HA/nSiO₂ nanocomposite scaffolds. The pore size and wall thickness can be adjusted frequently by increasing or decreasing the cooling rate during the freezing process, as previously reported in our recent reports [37, 43]. Figures 5 and 6 clearly indicate that increasing of cooling rate provides smaller pores and thinner walls. Higher cooling rates mean higher interface velocity (v) and thinner structural wavelength (λ) (average ice crystal thickness + entrapped particles thickness, see Fig. 7), and consequently finer lamellae structure according to:

$$\lambda \sim v^{-n},$$
 (5)

where λ is the structural wavelength, ν is the velocity of the ice front, and n depends on the particle size [51].

On the one hand, at the cooling rate of 4 °C/min, the water in the slurry reaches a supercooled state more rapidly compared to the cooling rate of 1 °C/min, and then higher amounts of ice crystals are formed. Because of the quick

freezing time, the ice crystal growth is suppressed and the smaller crystals are formed. On the other hand, at the cooling rate of 4 °C/min, compared to the cooling rate of 1 °C/min, the particles have less time to migrate and rearrange by diffusion mechanisms that lead to the formation of thinner walls [52]. In general, the finer structures could be attained by increasing the cooling rate. As it can be seen in Figs. 5 and 6 and depicted diagram in Fig. 8a, the pore size and wall thickness could be adjusted by replacing the microsize particles with the nanosize particles. As described in our previous work on HA/nAl₂O₃ nanocomposites, the smaller particle size addition results in the finer lamellae structures (Fig. 7), which is in a good agreement with the obtained results about the nanocomposite containing nSiO₂ and micro-HA particles [43]. In fact, increasing the particle size leading to elevation in n and v parameters and reduction in the structural wavelength according to Eq. (5), and in turn finer lamellae structures [53]. The increasing of v is due to the larger particles that in this case means smaller surface area. This smaller surface area provides few nucleation sites and concurrently lessens initial temperature for nucleation. Thus, the system moves in a progressively supercooled state which causes a faster interface velocity. In turn, the larger particles have less time for rearranging between the ice crystals, and there by thinner walls are formed [40].

Sintering temperature is another factor that influence the microstructure of $HA/nSiO_2$ nanocomposite scaffolds. In general, the pore size decreases with increasing the sintering temperature [43]. However, it is necessary to consider some points. Figure 9 shows the $HA/nSiO_2$

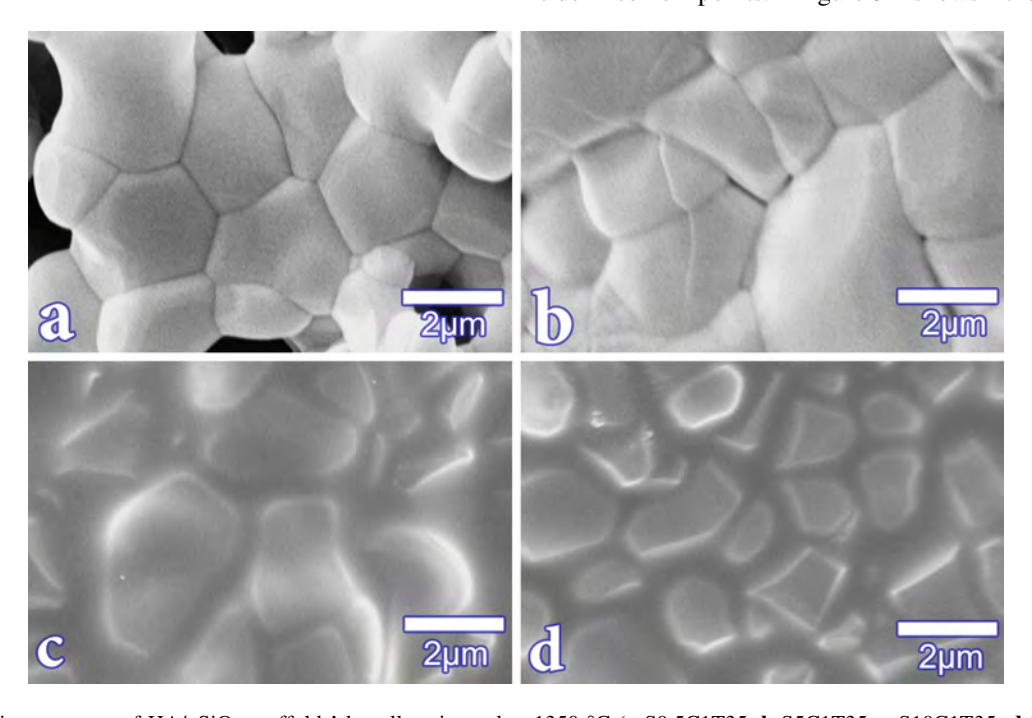


Fig. 10 The microstructure of HA/nSiO₂ scaffolds' lamellae sintered at 1350 °C (a S0.5C1T35, b S5C1T35, c S10C1T35, d S15C1T35)



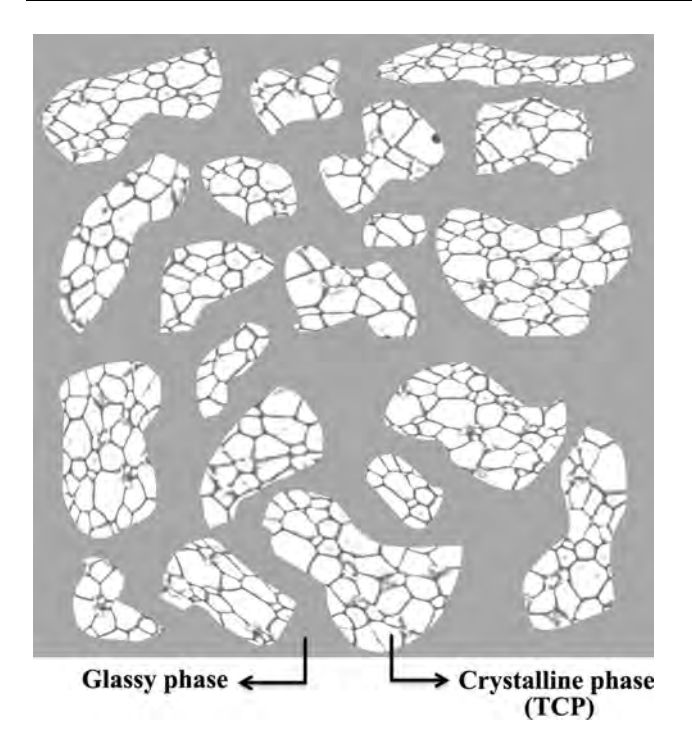


Fig. 11 Schematic image of microstructure of TCP grains in amorphous phase matrix

nanocomposite scaffolds and their horizontal and vertical cross section SEM micrographs, with different HA/nSiO₂ contents at cooling rate of 1 °C/min sintered at 1350 °C. Similar to 1200 °C, in the horizontal and vertical cross section SEM micrographs of scaffolds containing 0.5 and 5 vol% nSiO₂ sintered at temperature of 1350 °C, the pore size become larger with increasing the nSiO₂ content (Fig. 8b). But, further increase in the nSiO₂ content (S10C1T35, S15C1T35) induces severe shrinkage in the scaffolds; as a consequence, the pores are mostly closed or distorted.

Also, investigation of the microstructure of the scaffolds' lamellae demonstrated significant changes in grain boundaries with increasing of the nSiO2 content. The microstructure of the scaffold's lamellae, with different HA/nSiO₂ contents sintered at 1350 °C (S0.5C1T35, S5C1T35, S10C1T35, S15C1T35) are shown in Fig. 10. As shown in Fig. 10a, the microstructure of the scaffold containing 0.5 vol% nSiO₂ indicated clear demarcation in the grain boundaries. Also, the amount of microporosities was noticeable. By changing the amount of nSiO₂ from 0.5 to 5 vol%, the grain boundaries became slightly vague and show a high-densification behavior. With further increase in the nSiO₂ content (S10C1T35, S15C1T35), the microstructure of the scaffold's lamellae exhibited quite distinctive features. Figure 10c, d shows a bimodal structure in which, crystalline grains (α-TCP, β-TCP) surrounded with a matrix of amorphous phase. This microstructure, which is also plotted schematically in Fig. 11, confirms an amorphous phase formation in "Phase analysis" section.

Evaluation of mechanical strength

Table 2 shows the values of shrinkage, porosity, and compressive strength of all samples. As it can be seen, three factors have significant effects on the compressive strength of the HA/nSiO₂ nanocomposite scaffolds as the nSiO₂ content, the cooling rate, and the sintering temperature. By altering the processing parameters, properties such as porosity and pore size, shrinkage percentage, mechanical strength, and phase composition of final scaffolds can be regulated [37, 52]. Figure 12 shows porosity, shrinkage, and mechanical strength of the scaffolds as a function of nSiO₂ content at different cooling rates (1 and 4 °C/min) sintered at different temperatures (1200 and 1350 °C). At first in both cooling rate and sintering

Table 2 The shrinkage, porosity, and compressive strength of all samples

Sample code	Shrinkage (%)	Porosity (%)	Compressive strength (MPa)	Sample code	Shrinkage (%)	Porosity (%)	Compressive strength (MPa)
S0.5C1T20	18.33	84.43	0.36	S5C1T20	13.39	86.12	0.16
S0.5C4T20	17.86	84.66	0.53	S5C4T20	12.82	86.46	0.34
S0.5C1T35	48.82	78.05	2.68	S5C1T35	50.64	73.71	6.38
S0.5C4T35	48.07	78	5.66	S5C4T35	50.73	73.02	7.72
S1C1T20	15.58	85.19	0.24	S10C1T20	23.74	84.04	0.58
S1C4T20	16.78	84.96	0.46	S10C4T20	24.24	83.9	1.37
S1C1T35	43.02	79.52	2.58	S10C1T35	79.89	40.95	49.08
S1C4T35	42.26	79.09	4.67	S10C4T35	80.73	39.25	53.55
S1.5C1T20	16.68	85.82	0.22	S15C1T20	28.2	82	1.04
S1.5C4T20	16.45	85.83	0.42	S15C4T20	29.41	80.95	2.74
S1.5C1T35	41.16	79.7	2.15	S15C1T35	82.96	31.27	69.06
S1.5C4T35	40.88	80.71	4.1	S15C1T35	83.2	29.82	71.96



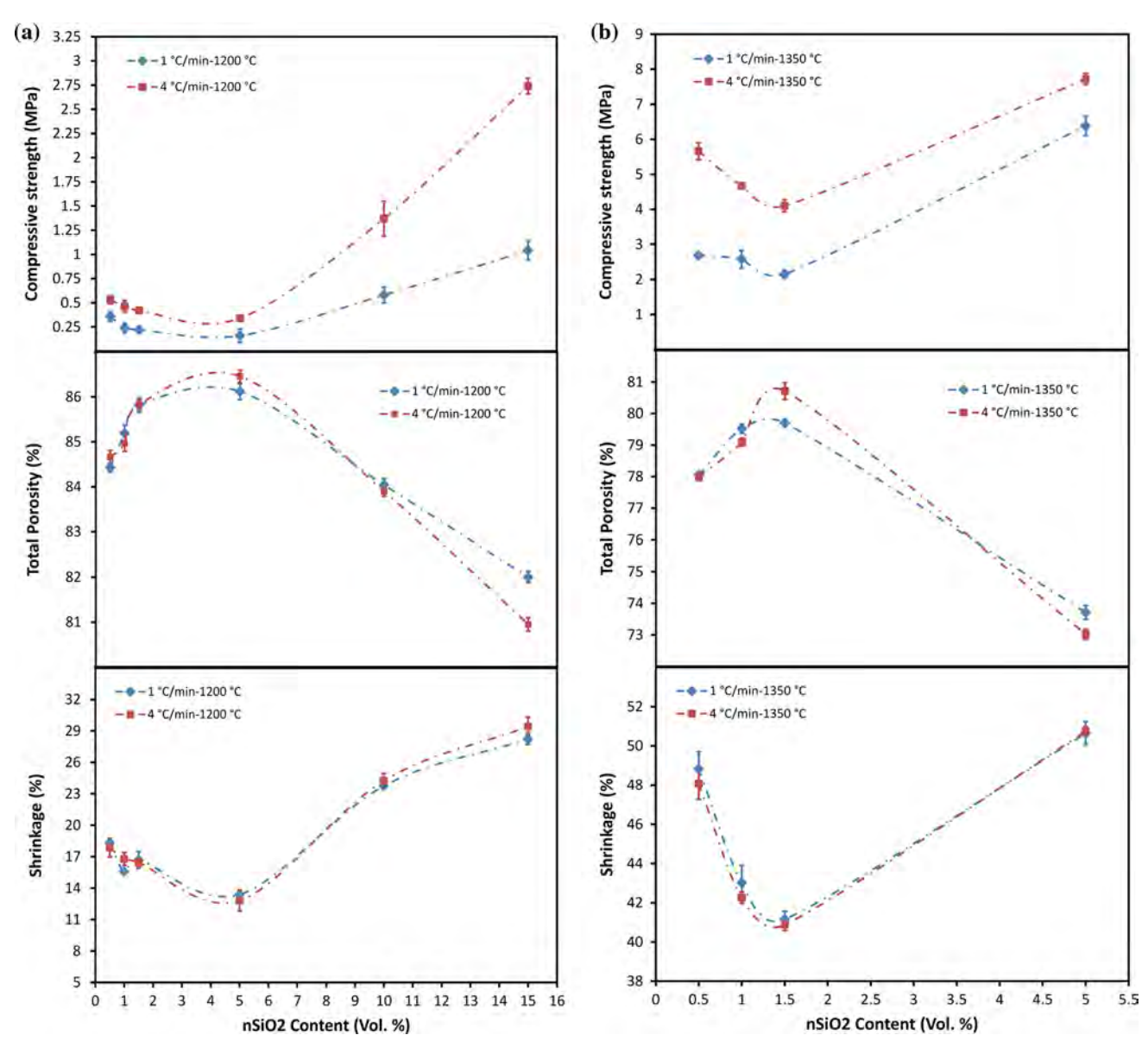


Fig. 12 Effect of nSiO₂ content on shrinkage, porosity, and compressive strength of HA/nSiO₂ nanocomposites at different cooling rates and sintering temperatures (a 1200 °C, b 1350 °C)

temperatures, the total porosity value increases with the elevation in the nSiO₂ contents. This is due to the reduction in volume shrinkage. Furthermore, it is clear that initially the compressive strength of the scaffolds decreases with rise in the nSiO₂ contents. The decomposition of HA to TCP phases as well as increasing the porosity can be the reasons of this reduction in the compressive strength. Although, with further addition of nSiO₂ in both cooling rate and sintering temperatures, the total porosity value decreased as volume shrinkage increased. Also due to reduced total porosity and calcium silicate or amorphous phase formation, the compressive strength of the scaffolds augments. Another important factor that has influence on

the compressive strength is cooling rate. As it can be seen in Fig. 12, in both sintering temperatures by increasing the cooling rate from 1 to 4 °C/min, the compressive strength fairly increased. With an elevation in the cooling rate, the pore size reduced because of the higher interface velocity (shorter freezing time), and consequently an enhancement in the compressive strength of the nanocomposite scaffolds was observed. The obtained results related to the correlation between the cooling rate and the compressive strength are in a good agreement with the reported data by other researchers [40, 52]. It should be noted that the cooling rate had no obvious influence on the shrinkage percentage and the total porosity.



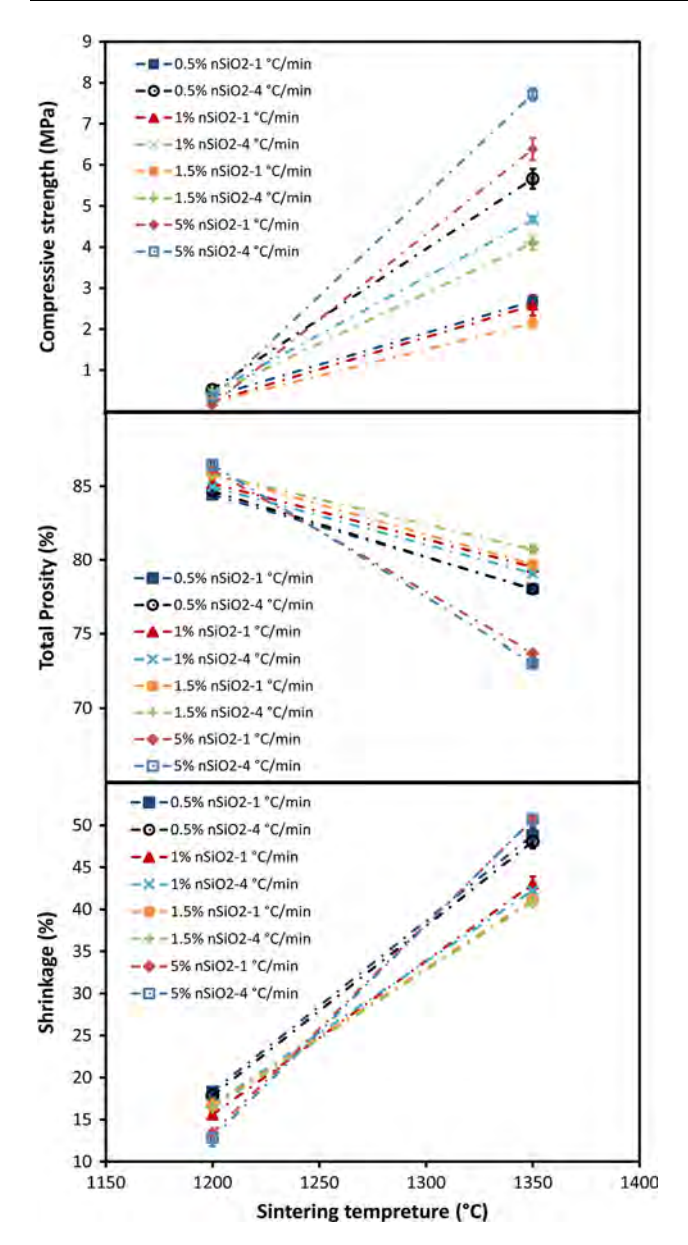


Fig. 13 Effect of sintering temperature on shrinkage, porosity, and compressive strength of $HA/nSiO_2$ nanocomposite scaffolds

As shown in Fig. 13, the shrinkage and the compressive strength increased as a function of sintering temperature, whereas the sintering temperature had verse effects on the total amount of porosity. According to the literature, by increasing the sintering temperature from 1200 to 1350 °C, the porosity descends and the shrinking value ascends, and as a result, the compressive strength increases [37, 52]. In total, optimal compressive strengths for this type of scaffolds can be attained by adjusting the nSiO₂ content, cooling rate, and sintering temperature. In a recent study, Zheng et al. [54] used bioglass to improve the mechanical strength of HA scaffolds, produced by a 3D printing method, and obtained a compressive strength of near

1.69 MPa and porosity around 72 % by adding 15 % bioglass to the HA matrix. In another work, Zhang et al. [55] fabricated HA scaffolds via the freeze casting method and obtained porosity values and compressive strength of 68 % and 2.4 MPa, respectively. As shown in Table 2, more desirable results were achieved compared to the reported data by other researchers with the same approximate amount of porosity.

Appropriateness as a bone substitute

The porosity, pore size, and compressive strength are the most critical features of biomaterial scaffolds. Several investigators have studied bone ingrowth into porous scaffolds with different pore sizes. The diameter of interconnecting pores seems to determine the quality of tissue growing into the porosity spaces. The minimum pore size that is required to generate mineralized bone is considered to be 40–100 µm [52, 56–58]. In addition, the scaffolding materials should have compressive strength as close as possible to the strength of cancellous bone (2–12 MPa) [59]. Thus, the HA/nSiO₂ nanocomposites with 5 % nSiO₂ and a cooling rate of 1 °C/min and sintering temperature of 1350 °C (S5C1T35), along with a porosity of 73 %, a compressive strength of 6.38 MPa, and a pore size of 224.4 µm in long axis and 40.89 µm in short axis, was chosen as an optimum sample.

Conclusions

Highly porous and open interconnected pore structural HA/nSiO₂ scaffolds were fabricated through freeze casting technique. The results showed that the phase composition is influenced by nSiO₂ content and sintering temperature in which HA decomposes to β-TCP or α-TCP. Moreover, Ca₂SiO₄ or an amorphous phase has formed as a reinforcing phase. By altering the processing parameters like nSiO₂, cooling rate, and sintering temperature, the scaffolds with total porosity of 30-86.5 % and compressive strength from 0.16 to 71.96 MPa were obtained. The porosity initially ascended and then descended as a function of the nSiO2 content whereas the nSiO₂ content had an opposite effect on the compressive strength. In addition, the pore size of the long and short axis lies between 121.9–420.3 and 15.7–66.1 µm, respectively, that increases with more nSiO₂ content and less cooling rate. Furthermore, increasing the sintering temperature from 1200 to 1350 °C decreases the pore size that this trend is more notable in the higher nSiO₂ content. The prepared scaffold with the mentioned characteristics has the potential to be a promising substitute for regeneration of damaged bone.



References

- Ohgushi H, Goldberg VM, Caplan AI (1989) Repair of bone defects with marrow cells and porous ceramic: experiments in rats. Acta Orthop 60:334–339
- Arvidson K, Abdallah BM, Applegate LA, Baldini N, Cenni E, Gomez-Barrena E, Granchi D, Kassem M, Konttinen YT, Mustafa K, Pioletti DP, Sillat T, Finne-Wistrand A (2011) Bone regeneration and stem cells. J Cell Mol Med 15:718–746
- Naderi H, Matin MM, Bahrami AR (2011) Review paper: critical issues in tissue engineering: biomaterials, cell sources, angiogenesis, and drug delivery systems. J Biomater Appl 26:383–417
- Stevens MM (2008) Biomaterials for bone tissue engineering. Mater Today 11:18–25
- Dorozhkin SV (2010) Bioceramics of calcium orthophosphates. Biomaterials 31:1465–1485
- Thamaraiselvi TV, Rajeswari S (2004) Biological evaluation of bioceramic materials-a review. Trends Biomater Artif Organs 18:9–17
- Hesaraki S, Zamanian A, Moztarzadeh F (2009) Effect of adding sodium hexametaphosphate liquefier on basic properties of calcium phosphate cements. J Biomed Mater Res A 88:314

 –321
- Zamanian A, Moztarzadeh F, Kordestani S, Hesaraki S, Tahriri MR (2010) Novel calcium hydroxide/nanohydroxyapatite composites for dental applications: in vitro study. Adv Appl Ceram 109:440–445
- Hesaraki S, Zamanian A, Khorami M (2011) Nano-structured apatite granules as drug delivery device for bone infection treatments. J Aust Ceram Soc 47:32–36
- Hesaraki S, Zamanian A, Nazarian H (2009) Physical and physicochemical evaluation of calcium phosphate cement made using human derived blood plasma. Adv Appl Ceram 108: 253–260
- Sung Y-M, Shin Y-K, Ryu J-J (2007) Preparation of hydroxyapatite/zirconia bioceramic nanocomposites for orthopaedic and dental prosthesis applications. Nanotechnology 18:065602
- Evis Z, Doremus RH (2007) A study of phase stability and mechanical properties of hydroxylapatite–nanosize α-alumina composites. Mater Sci Eng C 27:421–425
- Li X, Yasuda H, Umakoshi Y (2006) Bioactive ceramic composites sintered from hydroxyapatite and silica at 1200°C: preparation, microstructures and in vitro bone-like layer growth. J Mater Sci Mater Med 17:573–581
- Fidancevska E, Ruseska G, Bossert J, Lin Y-M, Boccaccini AR (2007) Fabrication and characterization of porous bioceramic composites based on hydroxyapatite and titania. Mater Chem Phys 103:95–100
- Muralithran G, Ramesh S (2000) The effects of sintering temperature on the properties of hydroxyapatite. Ceram Int 26:221–230
- Huaxia JI, Marqius PM (1993) Sintering behaviour of hydroxyapatite reinforced with 20 wt% Al₂O₃. J Mater Sci 28: 1941–1945. doi:10.1007/BF00595767
- Sayer M, Stratilatov AD, Reid J, Calderin L, Stott MJ, Yin X, MacKenzie M, Smith TJN, Hendry JA, Langstaff SD (2003) Structure and composition of silicon-stabilized tricalcium phosphate. Biomaterials 24:369–382
- Miao X, Lim W-K, Huang X, Chen Y (2005) Preparation and characterization of interpenetrating phased TCP/HA/PLGA composites. Mater Lett 59:4000–4005
- Ji H, Marquis PM (1992) Preparation and characterization of Al₂O₃ reinforced hydroxyapatite. Biomaterials 13:744–748
- Evis Z, Ergun C, Doremus RH (2005) Hydroxylapatite–zirconia composites: thermal stability of phases and sinterability as related to the CaO–ZrO₂ phase diagram. J Mater Sci 40:1127–1134. doi:10.1007/s10853-005-6928-y

- Guo H, Khor KA, Boey YC, Miao X (2003) Laminated and functionally graded hydroxyapatite/yttria stabilized tetragonal zirconia composites fabricated by spark plasma sintering. Biomaterials 24:667–675
- Juang HY, Hon MH (1994) Fabrication and mechanical properties of hydroxyapatite–alumina composites. Mater Sci Eng C 2:77–81
- An SH, Matsumoto T, Miyajima H, Nakahira A, Kim KH, Imazato S (2012) Porous zirconia/hydroxyapatite scaffolds for bone reconstruction. Dent Mater 28:1221–1231
- Blindow S, Pulkin M, Koch D, Grathwohl G, Rezwan K (2009)
 Hydroxyapatite/SiO₂ composites via freeze casting for bone tissue engineering. Adv Eng Mater 11:875–884
- Porter AE, Patel N, Skepper JN, Best SM, Bonfield W (2004) Effect of sintered silicate-substituted hydroxyapatite on remodelling processes at the bone-implant interface. Biomaterials 25:3303–3314
- Patel N, Brooks RA, Clarke MT, Lee PMT, Rushton N, Gibson IR, Best SM, Bonfield W (2005) In vivo assessment of hydroxyapatite and silicate-substituted hydroxyapatite granules using an ovine defect model. J Mater Sci Mater Med 16:429–440
- Andrade JC, Camilli JA, Kawachi EY, Bertran CA (2002)
 Behavior of dense and porous hydroxyapatite implants and tissue response in rat femoral defects. J Biomed Mater Res 62:30–36
- Patel N, Best SM, Bonfield W, Gibson IR, Hing KA, Damien E, Revell PA (2002) A comparative study on the in vivo behavior of hydroxyapatite and silicon substituted hydroxyapatite granules. J Mater Sci Mater Med 13:1199–1206
- Sopyan I, Fadli A, Mel M (2012) Porous alumina–hydroxyapatite composites through protein foaming–consolidation method.
 J Mech Behav Biomed Mater 8:86–98
- 30. Deville S (2010) Freeze-casting of porous biomaterials: structure, properties and opportunities. Materials 3:1913–1927
- 31. Hutmacher DW (2000) Scaffolds in tissue engineering bone and cartilage. Biomaterials 21:2529–2543
- Fook MVL, Fidéles T, Fook A, Aparecida A, Costa R (2009) Porous hydroxyapatite scaffolds by polymer sponge method. Key Eng Mater 396:703–706
- Chopra K, Mummery P, Derby B, Gough J (2012) Gel-cast glass– ceramic tissue scaffolds of controlled architecture produced via stereolithography of moulds. Biofabrication 4:045002
- 34. Zhang Y, Yokogawa Y, Feng X, Tao Y, Li Y (2010) Preparation and properties of bimodal porous apatite ceramics through slip casting using different hydroxyapatite powders. Ceram Int 36:107–113
- Dìaz A, Hampshire S (2004) Characterisation of porous silicon nitride materials produced with starch. J Eur Ceram Soc 24: 413–419
- Agrawal DK (1998) Microwave processing of ceramics. Curr Opin Solid State Mater Sci 3:480–485
- 37. Farhangdoust S, Zamanian A, Yasaei M, Khorami M (2013) The effect of processing parameters and solid concentration on the mechanical and microstructural properties of freeze-casted macroporous hydroxyapatite scaffolds. Mater Sci Eng C 33:453–460
- Deville S (2008) Freeze-casting of porous ceramics: a review of current achievements and issues. Adv Eng Mater 10:155–169
- Arabi N, Zamanian A (2013) Effect of cooling rate and gelatin concentration on the microstructural and mechanical properties of ice template gelatin scaffolds. Biotechnol Appl Biochem 60:573–579
- 40. Zamanian A, Farhangdoust S, Yasaei M, Khorami M, Hafezi M (2014) The effect of particle size on the mechanical and microstructural properties of freeze-casted macroporous hydroxyapatite scaffolds. Int J Appl Ceram Technol 11:12–21
- Wegst UG, Schecter M, Donius AE, Hunger PM (2010) Biomaterials by freeze casting. Philos Trans R Soc Lond A 368:2099–2121



 Zhang Y, Zuo K, Zeng Y-P (2009) Effects of gelatin addition on the microstructure of freeze-cast porous hydroxyapatite ceramics. Ceram Int 35:2151–2154

- Ghazanfari SMH, Zamanian A (2013) Phase transformation, microstructural and mechanical properties of hydroxyapatite/ alumina nanocomposite scaffolds produced by freeze casting. Ceram Int 39:9835–9844
- Mallick KK (2009) Freeze casting of porous bioactive glass and bioceramics. J Am Ceram Soc 92:S85–S94
- Heunisch A, Dellert A, Roosen A (2010) Effect of powder, binder and process parameters on anisotropic shrinkage in tape cast ceramic products. J Eur Ceram Soc 30:3397–3406
- Santos DS, Lopes FS, Ferreira DC, Manuela C (2009) Hydroxyapatite, biocompatible glass and silicon-based bone substitute, production process and applications of thereof. WO Patent 2.009,126,054
- Liao C-J, Lin F-H, Chen K-S, Sun J-S (1999) Thermal decomposition and reconstitution of hydroxyapatite in air atmosphere. Biomaterials 20:1807–1813
- 48. Phillips B, Muan A (1959) Phase equilibria in the system CaOiron oxide–SiO₂, in air. J Am Ceram Soc 42:413–423
- Reid JW, Pietak A, Sayer M, Dunfield D, Smith TJN (2005)
 Phase formation and evolution in the silicon substituted tricalcium phosphate/apatite system. Biomaterials 26:2887–2897
- Jaworski R, Pierlot C, Pawlowski L, Bigan M, Quivrin M (2008)
 Synthesis and preliminary tests of suspension plasma spraying of fine hydroxyapatite powder. J Therm Spray Technol 17:679–684

- Deville S, Saiz E, Tomsia AP (2007) Ice-templated porous alumina structures. Acta Mater 55:1965–1974
- Deville S, Saiz E, Tomsia AP (2006) Freeze casting of hydroxyapatite scaffolds for bone tissue engineering. Biomaterials 27:5480–5489
- Deville S, Maire E, Lasalle A, Bogner A, Gauthier C, Leloup J, Guizard C (2010) Influence of particle size on ice nucleation and growth during the ice-templating process. J Am Ceram Soc 93:2507–2510
- Zheng W (2011) Preparation and characterisation of tri-calcium phosphate scaffolds with tunnel-like macro-pores for bone tissue engineering. Master Dissertation, Queensland University of Technology
- Zhang Y, Zhou K, Bao Y, Zhang D (2013) Effects of rheological properties on ice-templated porous hydroxyapatite ceramics. Mater Sci Eng C 33:340–346
- Le Huec JC, Schaeverbeke T, Clement D, Faber J, Le Rebeller A (1995)
 Influence of porosity on the mechanical resistance of hydroxyapatite ceramics under compressive stress. Biomaterials 16:113–118
- Itala AI, Ylanen HO, Ekholm C, Karlsson KH, Aro HT (2001)
 Pore diameter of more than 100 micron is not requisite for bone ingrowth in rabbits. J Biomed Mater Res 58:679–683
- Klawitter JJ, Bagwell JG, Weinstein AM, Sauer BW (1976) An evaluation of bone growth into porous high density polyethylene. J Biomed Mater Res 10:311–323
- Hench LL, Wilson J (1993) An introduction to bioceramics.
 World Scientific, Singapore, pp 12–26

